Journal of Power Sources 214 (2012) 386–398

Contents lists available at SciVerse ScienceDirect

Journal of Power Sources

journal homepage: www.elsevier.com/locate/jpowsour

Influence of the microporous layer on carbon corrosion in the catalyst layer of a polymer electrolyte membrane fuel cell

Dusan Spernjak*, Joseph Fairweather, Rangachary Mukundan, Tommy Rockward, Rodney L. Borup

Los Alamos National Laboratory, P.O. Box 1663, MPA 11, MS D429, Los Alamos, NM 87545, United States

HIGHLIGHTS

- ► Accelerated Stress Testing (AST) for carbon corrosion in a segmented PEM fuel cell.
- ► Compared cathode Gas Diffusion Layers (GDLs) with and without a microporous layer.
- ► Cells with cathode MPL are more resistant to corrosion of the catalyst support.
- ► Current distribution with cathode MPL changes due to catalyst layer degradation.
- ► Without cathode MPL, GDL fibers cause localized thinning in the catalyst layer.

ARTICLE INFO

Article history:
Received 16 February 2012
Received in revised form
24 April 2012
Accepted 26 April 2012
Available online 4 May 2012

Keywords:
PEM fuel cell
Carbon corrosion
Catalyst layer
Microporous layer
Current distribution
Degradation mechanisms

ABSTRACT

Corrosion of the catalyst support reduces PEM fuel cell performance via catalyst layer (CL) degradation (loss of porosity, catalyst connectivity, and active catalyst surface area). Carbon corrosion was investigated in a segmented cell for cathode gas diffusion layers (GDLs) with and without a microporous layer (MPL) to investigate the spatial aspects of GDL effect on corrosion. The cells were aged *in situ* using an accelerated stress test (AST) for carbon-support corrosion consisting of consecutive holds at 1.3 V. Carbon corrosion was quantified by measuring CO_2 evolution during the AST.

Performance degradation was substantial both with and without cathode MPL, but the degradation of the CL after prolonged corrosion was lower in the presence of an MPL. This was corroborated by better cell performance, higher remaining Pt active area, lower kinetic losses and smaller Pt particle size. The cell with an MPL showed increasingly nonuniform current distribution with corrosion time, which is correlated to the distribution of the Pt particle growth across the active area. This cell also showed an increase in mass-transport resistance due to MPL degradation. Without an MPL, GDL carbon fibers caused localized thinning in the cathode CL, originating from the combined effects of compression and corrosion.

1. Introduction

Polymer electrolyte membrane (PEM) fuel cells are energy conversion devices which have shown great promise for automotive, stationary and portable power applications. Cost-effective commercialization of PEM fuel cells requires reductions in fuel cell cost and improvements in durability, however with a minimal impact on the state-of-the-art initial fuel cell performance. Thus, over the past decade, more research has been focused on improving the durability of the fuel cell systems and components [1–6]. Durability of the catalyst layer (CL) remains one of the primary challenges in developing PEM fuel cell systems with acceptable lifetimes.

Current US DOE durability targets for fuel cell systems (with defined acceptable degradation rate) are 5000 h (~7 months) for automotive and 40,000 h (~4.6 years) for stationary applications. Considering the time and cost required for real-time testing of system lifetimes (so called 'life tests'), there is an urgent need for establishing standardized protocols that allow screening the durability characteristics of component materials in a reasonable turnaround time. The goal is to decouple the degradation mechanisms and separately evaluate the degradation rates for individual cell components. Such an approach requires fundamental understanding of the degradation mechanisms. Several accelerated stress tests (ASTs) have been developed to enable rapid evaluation of degradation rates for individual components of a fuel cell system

* Corresponding author. Tel.: +1 302 229 0675; fax: +1 505 665 4292.
E-mail address: spernjak@lanl.gov (D. Spernjak).

0378-7753/$ – see front matter © 2012 Elsevier B.V. All rights reserved.
doi:10.1016/j.jpowsour.2012.04.086

[1,4,6–8]. Although these durability protocols are not yet fully standardized, four ASTs have been proposed to characterize the (i) catalyst (potential cycling); (ii) catalyst support (elevated voltage hold); (iii) membrane-electrode assembly (MEA) chemical stability (open-circuit operation); and (iv) membrane mechanical stability (relative humidity cycling). The ASTs are crucial for quantifying tradeoffs between the cost, durability and performance. In order to quantitatively correlate the degradation rates in real system testing (i.e. field data) to the accelerated stress testing [8], one needs to take into account the effects of additional stressors (e.g. start/stop, temperature, and relative humidity).

In this work we consider a catalyst layer commonly used in PEM fuel cells; a porous structure consisting of carbon-supported platinum catalyst in an ionomer matrix [9–12]. Corrosion of the catalyst support in PEM fuel cells reduces the overall cell performance as it leads to the loss of the active catalyst surface area and catalyst connectivity, and lowers the porosity and hydrophobicity of the catalyst layer [1–4,9,13,14]. Thus, carbon-support corrosion is a key degradation mechanism in PEM fuel cells.

Carbon corrosion in aqueous acid electrolyte (such as a proton-exchange membrane) is described by [15]:

$$C + 2H_2O \rightarrow CO_2 + 4H^+ + 4e^-, \quad E_0 = 0.207V_{RHE} \tag{1}$$

At sufficient anodic potential, carbon dioxide is produced from the complete oxidation of elemental carbon by water. Although the corrosion is accelerated by Pt catalyst [16], in the typical range of cathode potentials this reaction is slow due to low operating temperature of PEM fuel cells. However, certain areas of the cathode CL may experience high potentials (versus reference hydrogen electrode, RHE) during cell operation, yielding high corrosion rates which cause a major damage to the catalyst support. Such situations occur when the anode compartment of a single cell contains both hydrogen-starved and hydrogen-rich regions. Accelerated carbon corrosion proceeds locally in the cathode region corresponding to the hydrogen-starved region of the anode [17]. The proposed mechanism was termed 'the reverse-current mechanism' [18] as the H_2/air portion of the cell drives the reverse current in the hydrogen-starved region. During the steady-state operation, localized fuel starvation may occur due to anode flooding or flow maldistribution [17,19–21]. Patterson and Darling [17] simulated such a condition by restricting the hydrogen access in a small portion of the anode catalyst layer in a cell operating at 0.4 A cm^{-2} for 100 h. They demonstrated that the cathode CL corresponding to the hydrogen-depleted area suffered the loss of carbon and significant thinning.

Regions of the cathode CL may experience high-potential excursions not only during steady-state operation, caused by localized fuel starvation, but also during transient operation, i.e. cell startup and shutdown (SU/SD). A fuel/air boundary on the anode side of the cell during SU/SD operation can induce local potentials at the cathode typically as high as 1.2–1.5 V [18,22–26]. Although these transients are relatively short (residence time <0.1 s [27]), cumulative time at elevated potentials may cause significant damage to the CL in systems which require frequent startups and shutdowns, such as in automotive applications. The use of graphitized carbons as the catalyst support increases the CL resistance to carbon corrosion [7,26,28], however with the penalties of (i) higher material cost (thermal treatment in the fabrication process) and often (ii) lower initial performance (due to lower carbon surface area and consequently lower electrochemical catalyst surface area). Since the improvement in carbon-support stability will usually come at the expense of cost and/or initial performance, various system-level strategies have been proposed to mitigate the long-term effects of carbon corrosion [9].

Since the local conditions (such as humidity, temperature, and reactant composition) vary across the active area during cell operation, it is expected that different regions of the cell will experience varying rates of degradation. It is therefore important to provide spatially resolved measurements across the cell area to evaluate the degradation levels due to operational variables. Segmented cells have been used extensively as a diagnostic tool in a variety of fuel cell studies (e.g. mass-transport optimization, water and thermal management, flow field design and model validation) [29–31]. More recently, current distribution measurements have also shown to be invaluable in elucidating the degradation mechanisms [22,27,32–34]. By using an approach of simulated localized fuel starvation [17] in a segmented cell, Carter et al. [27,34] measured local polarization curves across the cell area. The hydrogen-starved region exhibited significantly reduced limiting current (due to oxygen mass-transport limit) compared to the rest of the cell. This localized performance degradation was correlated to the cathode CL thinning and the loss of active area due to carbon corrosion. Lamibrac et al. [27] reported higher CL degradation in the outlet region after repeated cell startups, by measuring the internal currents and EIS (electrochemical impedance spectroscopy). A visualization technique was employed by Ishigami et al. [32] to measure the distribution of oxygen partial pressure in the flow field and record the progression of H_2/air front during SU/SD operation. The inlet and especially outlet region were identified as critical regions that suffered higher levels of performance degradation due to CL damage during SU/SD cycling.

For the most part, carbon corrosion studies have focused on the catalyst support, i.e. carbon in the catalyst layer. The gas diffusion layer (GDL) and microporous layer (MPL) are often not considered as additional sources of carbon for the carbon corrosion reaction. However, the region of the GDL (or MPL) in direct contact with the CL is also susceptible to corrosion, as it experiences similar corrosive conditions (high potential, humidity, and O_2 concentration) in the proximity of Pt catalyst and electrolyte. The MPL, typically containing amorphous carbon, is more vulnerable than the graphitized carbon fibers in the GDL substrate. Owejan et al. [35] showed that using graphitized carbon, Pureblack® [36] instead of acetylene black in the MPL, reduced the performance degradation by more than 50% (at 0.6 V) after cumulative 25 h of AST at 1.2 V. The graphitized MPL also performed better at high current after SU/SD cycling, indicating mass-transport (*MT*) problems caused by corrosion in the acetylene black MPL. Note that it is challenging to distinguish between the performance degradation contributions due to mass-transport issues from carbon corrosion in the CL and carbon corrosion in the MPL.

Carbon corrosion (be it in the CL or the MPL) also makes the surfaces more hydrophilic via roughening and addition of oxide groups resulting in water management challenges [14]. In addition, pore collapse in the MPL after prolonged cell testing (~650 h) has been suggested from porosimetry measurements (increase in the small pore volume at the expense of the large pore volume) [37]. Although the degradation mechanisms of the GDL are not yet well understood, GDL materials subjected to various *ex situ* aging protocols exhibited loss of hydrophobicity [1,38,39]. Finally, while extensive research has focused on optimizing GDL and MPL for water management [19,20,40], more work is needed to elucidate the influence of the GDL material on long-term cell performance and corrosion in the CL.

The present study employs a segmented cell to measure spatial variations in performance degradation as a function of GDL material and AST time. The influence of the MPL on carbon corrosion was evaluated by characterizing the degradation using the same GDL carbon-fiber substrates with and without an MPL. The materials were aged *in situ* in a 50 cm^2 cell with a 10 by 10 segmented current

collector using an AST protocol for catalyst support, consisting of consecutive holds at 1.3 V in humidified H_2/N_2 at 80 °C. Carbon corrosion during potential steps was quantified by measuring the carbon dioxide content of the nitrogen exhaust stream, coming from the side that serves as the cathode during subsequent H_2/air operation (Section 3.1.1). Performance degradation was characterized *in situ* by cyclic voltammetry (Section 3.1.2), polarization curves, cell operation at fixed conditions, current distribution, and electrochemical impedance spectra (Section 3.1.3). *Ex situ* analyses were performed on new and aged MEAs to correlate the changes in Pt particle size, CL thickness, and material morphology to the performance degradation (Section 3.2). These results are useful in elucidating the influence of the MPL on carbon corrosion and CL durability.

2. Experimental

The cell hardware is depicted in Fig. 1, with metrics and materials summarized in Table 1. The flow field (Fig. 1a) was machined into a 3 mm thick graphite plate, and is comprised of 5-pass serpentine channels connected by the manifolds at the bends (instead of having individual serpentines). Cell orientation during operation was vertical (channels horizontal, manifolds vertical), with inlets at the top (as indicated in Fig. 1). Compression of the cell was controlled by a fixture with a pneumatic actuator (BalticFuel-Cells GmbH). Temperature of the cell was controlled by (i) three cartridge heaters in each endplate and (ii) cooling plates adjacent to the endplates.

Current distribution was recorded using a 10 by 10 segmented current collector (Fig. 1b) and a printed-circuit board (S++ Simulation Services). The cathode current collector was the only segmented component of the cell, while the flow field, GDL, and MEA were all continuous. Although some minor smearing of the current distribution signal is expected due to the in-plane current flow, such a nonintrusive design eliminates the issues characteristic for cells with higher levels of segmentation [29,30] (e.g. disruptions in the fluid flow and sealing problems) while providing sufficient resolution on the cell scale. Current density measurements were spatially resolved at a length scale of ~7 mm.

Two types of GDL materials (by SGL Technologies GmbH) were used on the cathode side:

(i) SGL®24BA (carbon-fiber substrate only, 5% wt. PTFE, without the MPL), and
(ii) SGL®24BC (same carbon-fiber substrate as in SGL®24BA, but with an MPL, 23% wt. PTFE).

Table 1
Fuel cell metrics and materials.

Cell area	50 cm^2
Flow field	5-pass serpentine with manifolds
Channel	1 mm wide, 1 mm deep
Land	1 mm wide
MEA	GORE® PRIMEA® A510.2/M710.18/C510.4
Anode GDL	SGL®24BC (with MPL)
"BC cell" cathode GDL	SGL®24BC (with MPL)
"BA cell" cathode GDL	SGL®24BA (without MPL)

We refer to the above two cases as (i) the "BA cell" and (ii) the "BC cell".

The Anode GDL and the MEA were kept identical in all tests. SGL®24BC was used as the anode GDL. The MEAs (i.e. catalyst-coated membranes) were commercial GORE® PRIMEA® MEAs with 510 catalyst layers and a 710 membrane, with the anode/cathode Pt loading of 0.2/0.4 mg cm^{-2}.

Operating conditions for the cell characterization protocol, cyclic voltammetry, and AST for carbon corrosion are given in Table 2. Cells were subjected to the corrosion AST for a total of 7 h, with typical duration of each corrosion step (voltage hold at 1.3 V) of 1 h. This particular voltage was chosen to shorten the total test duration compared to standard carbon corrosion ASTs with 1.2 V [2,41] and to match the conditions of previously published experimental results [42]. Under identical settings (AST conditions, cell hardware, and BC cell materials), the performance decay was roughly eight times faster at 1.3 V than at 1.2 V. Namely, similar performance degradation at a cell current of 1.2 A cm^{-2} was observed after 24 h at 1.2 V (six consecutive 4 h holds) and after only 3 h at 1.3 V. Since carbon corrosion generally increases with relative humidity [43], the AST at saturated gas flows represents the worst-case scenario for catalyst support degradation.

To quantify carbon corrosion during each AST potential hold, a non-dispersive infrared (NDIR) sensor was used to measure the CO_2 content of the cathode exhaust (NDIR gas analyzer 603D by California Analytical Instruments, with dual range of 50 and 500 ppm and resolution of 1% of the range). The air entering the cell was scrubbed-free of carbon dioxide to allow accurate measurements of small CO_2 concentrations. As the NDIR measurement is disrupted by water in the gas stream, the air from the cell outlet was passed through a water trap (condenser) and a desiccant column before entering the NDIR instrument. The NDIR signal was integrated with time to calculate the total carbon that was fully oxidized (Fig. 2). This does not quite include all the carbon mass affected by corrosive conditions, since a portion of the surface is also expected to be partially oxidized without releasing CO_2 [14].

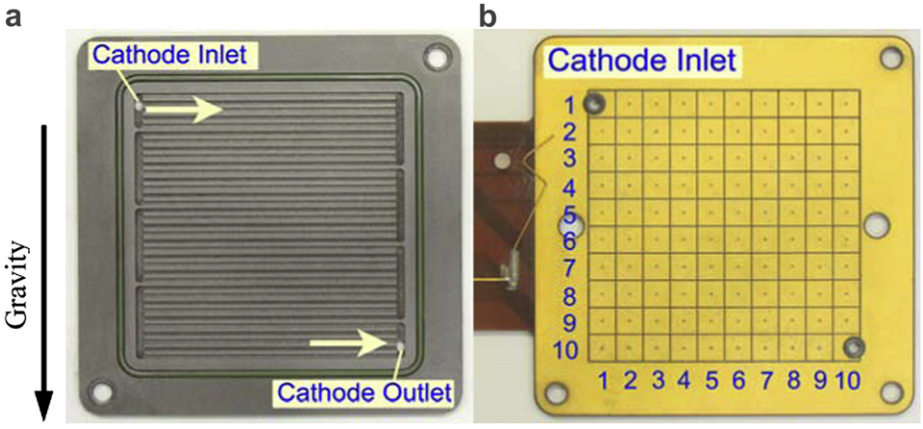

Fig. 1. Fuel cell hardware. (a) Cathode flow field. (Anode flow field is the mirror image of the cathode side, with the anode inlet in the top right corner, outlet in the bottom left corner). (b) Segmented current collector (10 by 10 segments).

Table 2
Operating conditions.

Condition/test type	Cell operation	Corrosion (1.3 V)	CV (ECSA)
Cell temperature (°C)	80	80	80
Humidifier temperature (°C)	80	80	80
Gases anode/cathode	H_2/air	H_2/N_2	H_2/N_2
Flow rates anode/cathode	Stoich. 1.2/2.0	200/75 sccm	500/500 sccm
Backpressure (kPa abs)	275	150	275

The cells were characterized *in situ*, at the beginning of life (BOL) and after each corrosion step, as follows: cyclic voltammogramms (CVs) were recorded at a scan rate of 20 mV s^{-1} (range 0.06–1.0 V vs. RHE) using potentiostat 273A by Princeton Applied Research (also used for the AST potential holds). The electrochemical active surface area (ECSA), Fig. 3, was calculated from the hydrogen desorption peak. Each CV measurement included three consecutive voltage sweeps, the averages of 2nd and 3rd sweep from each measurement are reported in Fig. 3.

The test protocol for characterizing the cell performance consisted of (i) polarization curves, i.e. VIRs (at the start and end of each protocol), (ii) 1 h operation at fixed conditions, and (iii) electrochemical impedance spectra (EIS). The polarization curves were recorded with decreasing and increasing voltage: Each curve in Fig. 4 is an average of four voltage sweeps between OCV and 0.4 V (two pairs of decreasing/increasing sweeps). Current distribution was measured while the cell was operated at fixed conditions, 0.1 A cm^{-2}, 1.2 A cm^{-2} (Figs. 5 and 6), and 0.6 V. Values shown in Figs. 5 and 6 were averaged over the last 5 min of 1 h long cell operation at fixed conditions. Electrochemical impedance spectra were recorded at 0.9 V (kinetic regime) and 1.2 A cm^{-2} (mass-transport regime), in the range from 0.1 Hz to 10 kHz (Figs. 7 and 8). Electronic load and gas flow, pressure, temperature, and humidity were controlled and monitored by a test station from Fuel Cell Technologies. The fuel cell test data are shown without applying an IR correction. The ohmic resistance for this particular cell hardware is higher than in a standard fuel cell setup. This yielded a high-frequency resistance (*HFR*) of ~0.14 Ω cm^2, compared to the typical *HFR* of around 0.04 Ω cm^2 measured in previous single-cell experiments without a pneumatic cell fixture [44]. This higher ohmic resistance is due to the pneumatic fixture (primarily from contact resistances between the fixture plates), rather than to the use of the segmented current collector.

Finally, new and tested (or, aged) MEAs were subjected to *ex situ* analyses. Samples were cut from selected areas of the aged MEAs to correlate the *ex situ* observations to the spatial trends in performance degradation. Pt particle size (Fig. 9) was measured using X-ray diffractometry (XRD) (Siemens D5000, Cu k-α radiation). The data were fit using whole-pattern fitting methods (Shadow analysis software from MDI Inc.) with particle size and strain line broadening functions [1,45]. The MEA area for each sample corresponded to ~3 × 3 current-collecting segments. The samples were prepared by carefully removing the GDLs and scraping the catalyst layer from catalyst-coated membranes. Next, micro X-ray computed tomography (microXCT) [46] was employed to visualize changes in the internal morphology of the MEAs before and after carbon corrosion (Fig. 10). Tomographic image sets of different regions of aged MEAs were recorded using a MicroXCT system (Xradia, Inc.) with a resolution of ~2 μm and a field of view of 1 by 1 mm. MEA cross-sections were imaged using a scanning electron microscope (SEM) to evaluate the thicknesses of the MEA components (Figs. 10 and 11). The samples were cut in a liquid-nitrogen bath to ensure clean cross-sectional images.

3. Results and discussion

3.1. In situ characterization

Carbon corrosion was induced by a series of 1 h AST potential holds at 1.3 V (total 7 h). Initial tests showed no significant performance changes after the first hour, therefore in subsequent tests we started with a 2 h corrosion step followed by a series of 1 h steps. Carbon corrosion was quantified by NDIR measurements of CO_2 evolved during potential holds, discussed in Section 3.1.1. *In situ* characterization was performed after each AST potential hold. The characterization protocol included ECSA measurements, presented in Section 3.1.2, as well as VIRs and current distribution measurements, discussed in Section 3.1.3. The changes in material morphology caused by carbon corrosion were analyzed *ex situ* using XRD, SEM, and XCT in Section 3.2.

3.1.1. Quantifying carbon corrosion

To quantify carbon corrosion, the carbon dioxide content of the nitrogen exhaust stream (cathode side during subsequent H_2/air fuel cell operation) was measured by NDIR during the potential holds. The total mass of carbon (μg C) fully oxidized to CO_2 was calculated by integrating the NDIR signal (ppm CO_2) with respect to time and assuming ideal gas behavior for converting exhaust flow rate:

$$\langle \mu g\ C \rangle = \frac{A_C Q_{std} P_{std}}{R T_{std}} \times \int \langle ppm\ CO_2 \rangle\, dt \quad (2)$$

where A_C is the atomic weight of carbon (12.01 g mol^{-1}), Q_{std} is the total volumetric flow rate under standard conditions (slpm), P_{std} is standard pressure (1 atm), R is the ideal gas constant (8.206×10^{-2} L atm K^{-1} mol^{-1}), T_{std} is standard temperature (273.15 K), and t is time (min).

Typical NDIR plots in Fig. 2a show the pattern of CO_2 release with time (each potential hold is from 0 s to 3600 s). There are distinctive peaks at both the start and end of each potential hold; CO_2 is rapidly released both when the potential is raised to +1.3 V and when it is lowered back to OCV (around +0.06 V for these cells under H_2/N_2). This agrees with previous observations combining cyclic voltammetry and exhaust analysis [16,43,47], where separate CO_2 release mechanisms have been identified for anodic vs. cathodic potential sweeps. The peak delay and spread at the start and end of each potential hold is caused by dead volume between the cell exhaust and the NDIR sensor (specifically the water trap). We also conducted tests with significantly less dead volume, which resulted in narrow, higher start/end peaks. However, such a setup required frequent desiccant replacements and system drainage without affecting the cumulative amount of CO_2 for the duration of a potential hold.

The amount of carbon oxidation decreases with each potential hold, reflecting the depletion of readily-oxidizable carbon in the cell. The surfaces in intimate contact with platinum particles are expected to be corroded fastest, as the reaction is catalyzed by platinum [16]. Carbon structures also contain a mixture of more graphitic and more amorphous regions, with the amorphous regions being more susceptible to oxidation [26]. Thus, as the more readily-oxidizable carbon (more amorphous and/or in direct contact with Pt) is removed, the overall amount of oxidation decreases.

The cumulative carbon oxidized to CO_2 from the two cells is shown in Fig. 2b. Two BA cells plotted together show a reasonable repeatability in carbon corrosion measurements. The difference between the BC and BA cells is small, with the BC cell showing more corroded carbon during the first 5 h of AST (7% higher than the BA

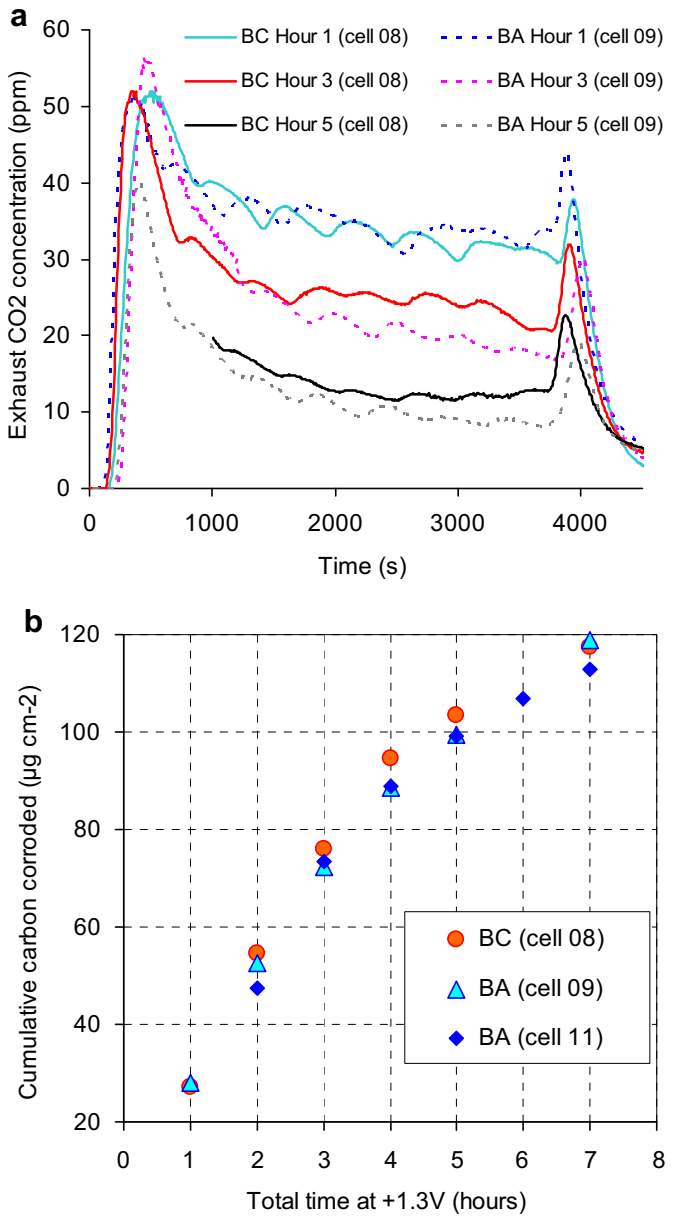

Fig. 2. Carbon corrosion as indicated by NDIR data for the two cathode GDL types. (a) CO_2 concentration in the cathode exhaust for three representative 1-h potential holds at +1.3 V (the beginning of hour 5 for the BC cell was lost due to an improperly installed water trap, but is otherwise representative). (b) Cumulative carbon corroded as calculated from integrated NDIR signal.

after 4 h). However, as will be shown in Sections 3.1.2 and 3.1.3, the BC cell had higher remaining ECSA and lower kinetic losses after prolonged corrosion, which indicates that the catalyst layer in the BC cell lost less carbon, i.e. that a portion of the evolved CO_2 originated from the MPL.

To confirm this hypothesis, additional shorter corrosion tests were performed with two different catalyst layers to independently assess the oxidation of the catalyst support and the MPL (Table 3). The GDLs were the same as in the BC cell (i.e. SGL®24BC on both sides). The first cell had the same series GORE® PRIMEA® MEA as indicated in Table 1, but with a lower catalyst loading of 0.1/0.2 mg Pt cm^{-2} on anode/cathode. This case served as a representative carbon-supported cathode catalyst layer. The second MEA was fabricated by painting Pt black catalyst layers (no carbon support) onto a Nafion® 112 membrane with a loading of 2 mg Pt cm^{-2} on each side and served as a representative of a carbon-free MEA. The tests were carried out in a 50 cm^2 gold-coated metallic hardware with single-serpentine flow field.

Table 3
Carbon oxidized to CO_2 in 5 min following a potential step from 0.0 V to the indicated potential. Conditions: 80 °C, 100% RH, H_2/N_2.

	1.0 V	1.2 V
GORE® PRIMEA® MEA (µg cm^{-2})	1.69	1.86
Pt black MEA (µg cm^{-2})	0.19	0.23
Portion of CO_2 from MPL	11%	13%

Estimates of total carbon oxidized in 5-min potential steps to 1.0 and 1.2 V are shown in Table 3. The cell with GORE® PRIMEA® MEA shows a total CO_2 release corresponding to well over 1 µg cm^{-2} of carbon following a single potential step. Assuming a composition of 50% Pt/C, the total loading of carbon is only 200 µg cm^{-2} in the GORE® PRIMEA® cathode layer, and nearly 1 wt.% of the support carbon appears to be lost in a single potential excursion. For comparison, a variety of catalyst supports have been shown to result in unacceptable performance losses when 9 to 14 wt.% was lost to corrosion [26].

The Pt black MEA shows a much smaller (although not negligible) CO_2 release, as expected due to the absence of carbon in the catalyst layer. Since no carbon support is included in the cathode layer of this cell, the corroded carbon is expected to come only from the GDL; mainly from the microporous layer. The released CO_2 is 11–13% of that in the GORE® PRIMEA® MEA case, implying that roughly one tenth of the signal in the GORE® PRIMEA® MEA case could come from the cathode MPL. Using the difference in areal weight between Sigracet® 24BA and 24BC GDLs (and subtracting 23 wt.% PTFE content), the MPL contains approximately 2.4 mg cm^{-2} carbon (i.e. there is roughly 10 times more carbon in the MPL than in the CL). Assuming the MPL contribution to the evolved CO_2 remains similar throughout the AST series (Fig. 2), cumulative amount of corroded MPL carbon is only ~0.5%. Although the portion of MPL corroded is quite small, this can still contribute significantly to mass-transport losses over cell lifetime [35,42].

3.1.2. Loss of electrochemical active surface area induced by carbon corrosion AST

Loss of platinum surface area was evaluated periodically during the carbon corrosion AST series to help understand the performance degradation mechanisms. The remaining normalized percentage of Pt ECSA after each corrosion step is shown in Fig. 3 for repeated tests with BC and BA cells. The initial (BOL) active surface area was measured to be 60 m^2_{Pt} g^{-1}_{Pt}. During the first hour of corrosion, the ECSA was reduced by 15%; however there was no change in the VIR performance. The delay in cell degradation with relatively high Pt loading (as used in the present work) indicates there is additional platinum which is initially not fully utilized, which can be lost without any notable performance loss, as shown in [41]. However, unless a more corrosion-resistant catalyst support is used, this reserve would probably not be sufficient to postpone the early performance degradation with lower Pt loading.

The difference in the ECSA loss rates between the two GDLs over the first 4 h is subtle. The ECSA of the BA cell (no MPL) decreases at a slightly higher rate than the BC cell during the first 2 h of corrosion. There may also be a temporary slowing of ECSA loss in the BA cells after 3 h of corrosion, but more data would be required to confirm this trend. The ECSA loss rate for the BC cell decreases more steadily throughout the test. Polynomial fits are included in Fig. 3 to help indicate the ECSA loss trends vs. corrosion time.

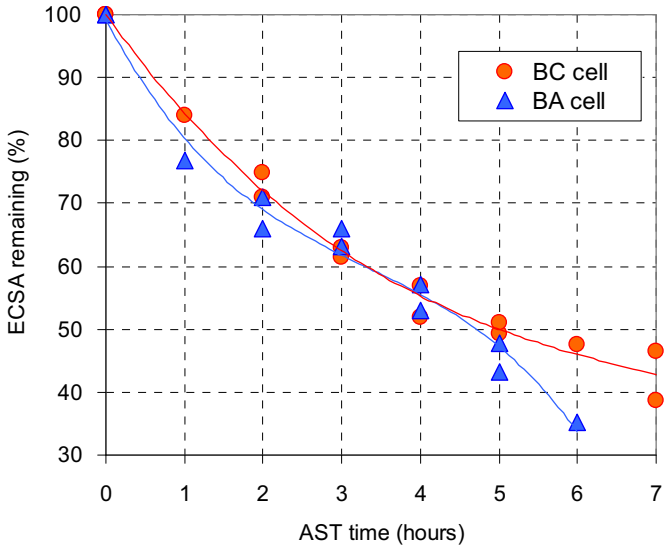

Fig. 3. Time evolution of the ECSA during the AST series for carbon-support corrosion (calculated from the hydrogen desorption peak on cyclic voltammogramms). Solid lines represent 3rd order polynomial fits. Average initial ECSA=60 $m^2_{Pt}\,g^{-1}_{Pt}$. CV conditions shown in Table 2.

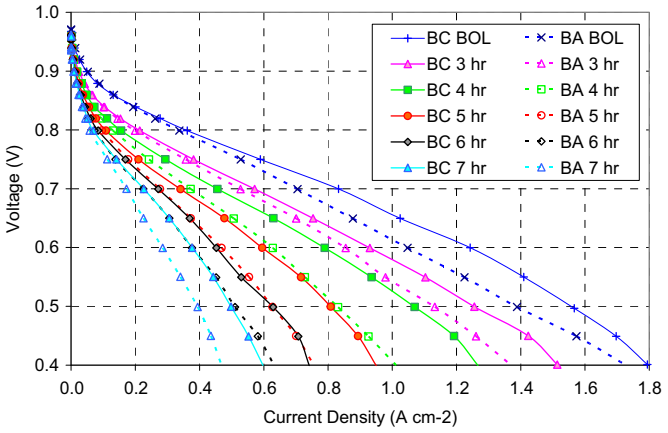

Fig. 4. Polarization curves at different times during AST series for two types of cathode GDLs. Operating conditions given in Table 2. BC cell (with MPL) are solid lines. BA cell (no MPL) are dashed lines.

The main feature in Fig. 3 is the increasing divergence of the remaining ECSAs between the BC and the BA cell following the 5th hour of AST. The rate of the ECSA loss is lower for the MPL case, while it seems to increase for the BA cell. The final remaining ECSA for the BA cell indicates that the ECSA would almost vanish within 2 additional hours of corrosion. However, the BC cell appears to be approaching a limiting surface area (although at already greatly reduced ECSA). After 6 h of corrosion, there is ~45% ECSA remaining in the BC cell, compared to ~35% remaining in the BA cell. The presence of MPL appears to have reduced the corrosion rates during AST by keeping the water levels in the catalyst layer lower than in the BA catalyst layer. Both cases displayed a dramatic loss of the active area: 5 h of corrosion at 1.3 V reduced the ECSA by more than 50%.

The BA cells exhibited increasing crossover throughout corrosion AST and possibly some electronic shorting during the 7th hour that makes the voltammetry difficult to analyze. For this reason the cyclic voltammetry for the BA cell after 7 h of AST was omitted in Fig. 3, because it required a current that exceeded the potentiostat limit. The increasing crossover was consistent with a gradual decrease in open-circuit voltage of ~0.02 V total after 6 h (followed by an additional >0.01 V drop during the 7th hour). The crossover and shorting issue in the absence of the cathode MPL will be revisited in Section 3.2. Open-circuit voltage for the BC cell (with the MPL) remained unchanged during the AST series.

3.1.3. Performance degradation

After each corrosion step, the gases were switched from H_2/N_2 to H_2/air and cell performance was characterized by polarization curves (VIRs), shown in Fig. 4, using conditions given in Table 2. Performance of the BA cell (dashed lines) remained inferior to that of the BC cell (solid lines) throughout the corrosion series, including the beginning of life (BOL) performance. Over the 7 h corrosion period, current density at 0.4 V was reduced by a factor of 3 for the BC cell and by a factor of 3.7 for the BA cell. Repeated tests (not shown) gave good repeatability: the BOL and 6–7 h curves were similar, while the polarization curves in between (1st through 5th hour) showed larger variations of up to ~15% in the current density at 0.4 V.

In addition, cells were tested at fixed operating conditions for 1 h (Figs. 5 and 6), at low current (0.1 A cm^{-2}) and at relatively high

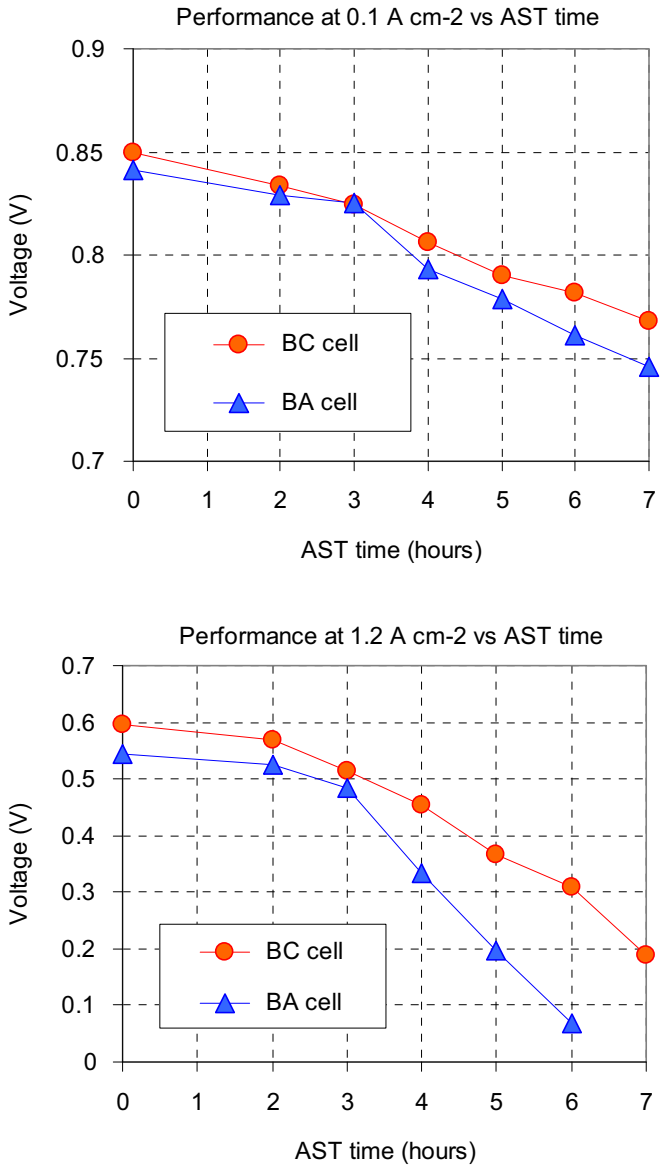

Fig. 5. Cell performance at 0.1 A cm^{-2} (top) and 1.2 A cm^{-2} (bottom) during corrosion ASTs for two types of cathode GDLs. Operating conditions given in Table 2.

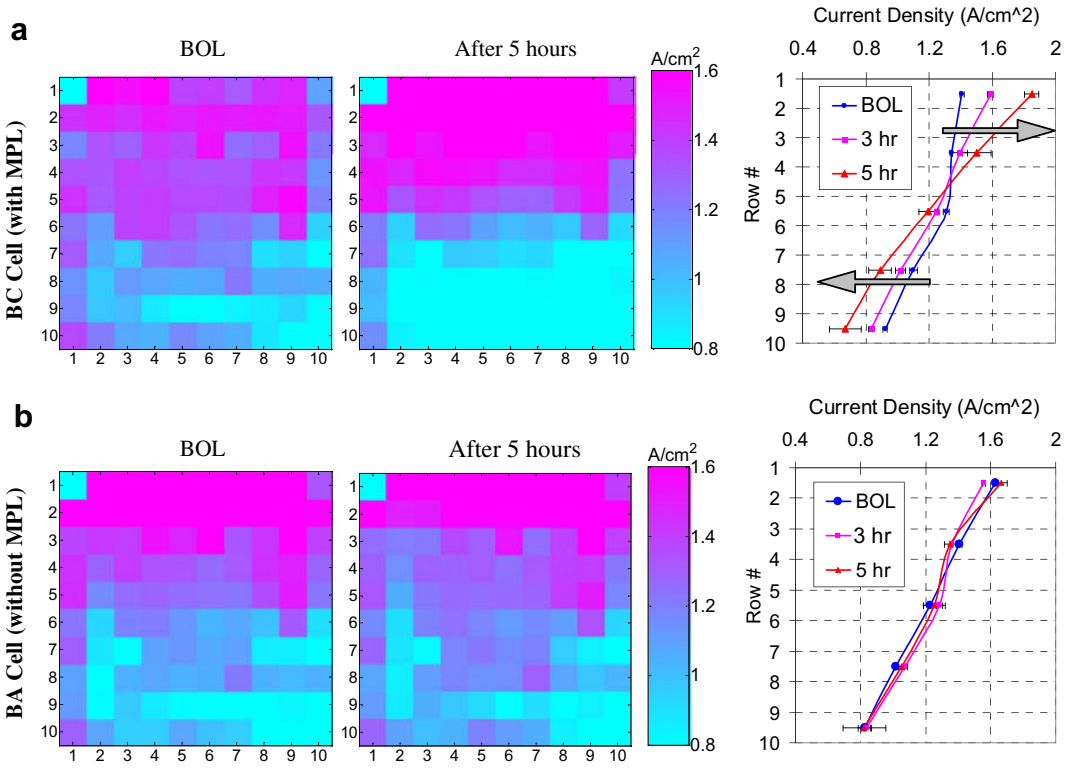

Fig. 6. Current density distributions at 1.2 A cm^{-2} vs. corrosion time: initial (BOL) and after 5 h of corrosion. Graphs on the right show the 1-D current distribution for BOL, and after 3 and 5 h of corrosion. Each data point is an average of two consecutive rows of segments. Error bars are +/− standard deviation from repeated aging experiments. Cell orientation and inlet/outlet locations shown in Fig. 1, voltages given in Fig. 5, conditions in Table 2. (a) Top row: BC cell (with MPL). (b) Bottom row: BA cell (without MPL).

current (1.2 A cm^{-2}). Over the first 3 h of the AST series, performance degradation is similar for the two GDL types. Trends in voltage degradation (Fig. 5) in the remainder of the AST protocol display a much higher loss rate in the BA cell, somewhat similar to the ECSA degradation at prolonged corrosion (Fig. 3). Further, temporal voltage fluctuations increased with the corrosion time in both cases, especially at a higher current density. This increasingly unstable cell operation can be attributed to mass-transport issues caused by carbon corrosion. In addition, gas maldistribution is likely to occur due to inferior liquid water removal for the given flow-field geometry [21]. Nonetheless, the BC cells were able to sustain 1.2 A cm^{-2} even after 7 h of corrosion, due to the better water management with an MPL and possibly also due to a lower level of CL degradation. The BA cells could not achieve 1.2 A cm^{-2} after the 7th hour.

Spatial current distributions were recorded throughout the tests at fixed conditions discussed above. Fig. 6 compares the current density distributions at 1.2 A cm^{-2} for the BC cell (Fig. 6a) and the BA cell (Fig. 6b), at BOL and after 5 h of corrosion AST. The corresponding voltage degradation data is given in Fig. 5. The elements in the 10 by 10 current distribution matrices correspond to the current-collecting segments (see Fig. 1). Corresponding to the colored distribution plots, the values in the matrix rows were averaged and plotted as 1-D current distributions going from inlet (row 1) to outlet (row 10) in Fig. 6, right hand side.

The BOL current distributions displayed the same trend with both GDL materials, showing high current in the inlet region and low current in the outlet region. At the BOL, the BC cell had more uniform distribution in which the local current density decreased in the flow direction from ∼1.4 A cm^{-2} at the inlet to ∼0.9 A cm^{-2} at the outlet. Local current in the BA cell varied between ∼1.6 A cm^{-2} and ∼0.8 A cm^{-2}. The decreasing trend in local current from inlet to outlet is reasonable considering the variations in the current density across the flow field were influenced by the downstream decrease in oxygen concentration caused by consumption due to reaction and dilution caused by water production [27,48]. Fully humidified gases in a co-flow arrangement were chosen to simplify the variations in local conditions across the cell (e.g. humidity and membrane hydration).

The current distribution in the BA cell remains unchanged during corrosion (Fig. 6b). The curves denoting the 1-D current distribution in the BA cell after 3 and 5 h are almost identical to the BOL distribution (and are similar to the distribution in the BC cell after 3 h of AST). Since the current distribution in the absence of the MPL remained unaffected by carbon corrosion, it can be inferred that the degradation rates were uniform across the active area of the BA cell. In contrast, the MPL case exhibits notable change in current distribution with corrosion time. Compared to the BOL distribution, local current density in corroded BC cells increased in the inlet region, and decreased in the outlet region (as indicated by arrows in Fig. 6). The divergence between the current density in inlet and outlet regions became higher with AST time. Such redistribution of the current density suggests that the BC cell did not degrade uniformly across the cell area, and that the outlet region suffered higher levels of degradation. Finally, current distributions at low current, 0.1 A cm^{-2} (not shown), exhibited similar trends to those observed at 1.2 A cm^{-2}, both at BOL and after corrosion.

Next, EIS measurements were employed to better distinguish between different mechanisms responsible for the performance degradation observed in the polarization curves. Impedance spectra, presented in Fig. 7a and b, are modeled using equivalent circuit shown in Fig. 7c (solid lines for the BC cell, dashed lines for the BA cell). Fitting was done using constant phase element [49],

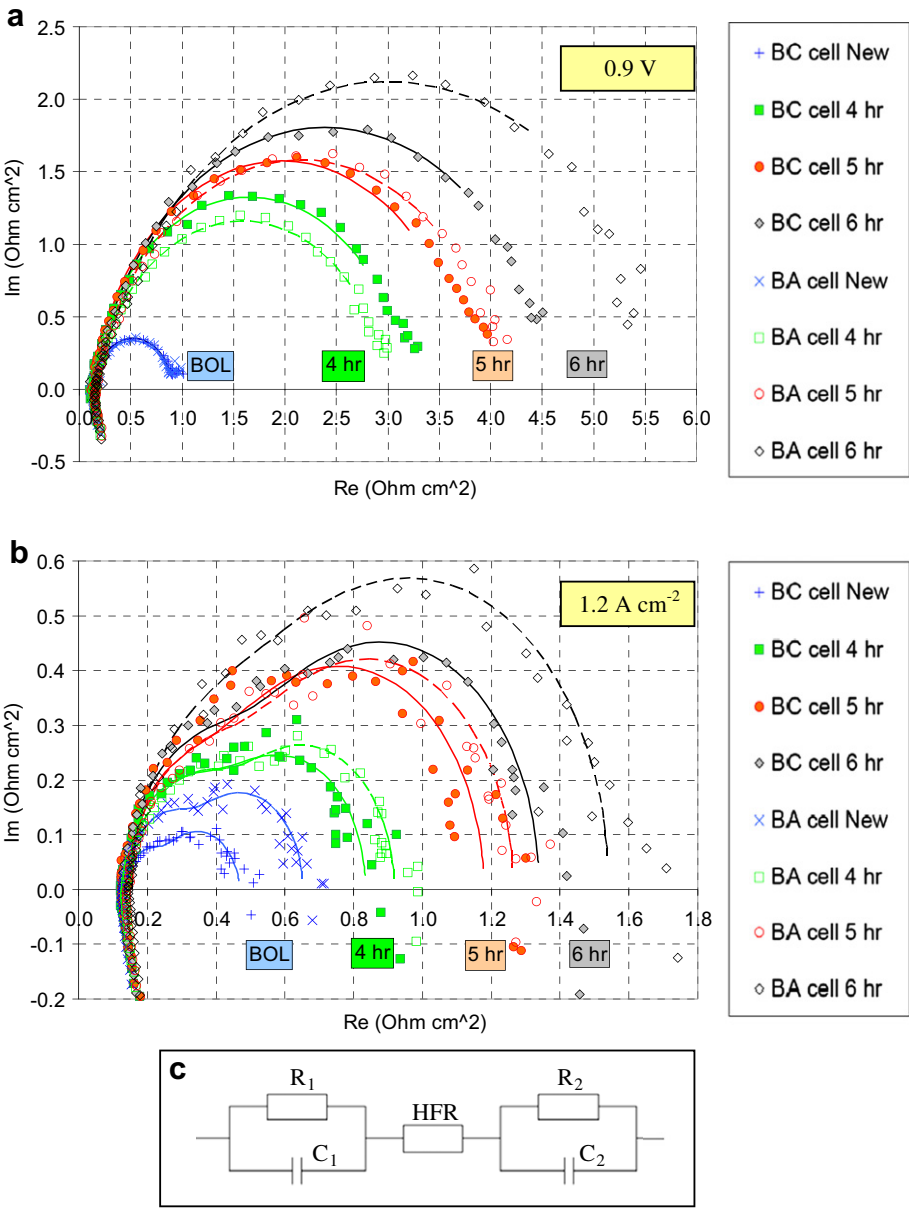

Fig. 7. Electrochemical impedance spectra (0.1 Hz–10 kHz) during the AST series for carbon-support corrosion for two types of cathode GDLs, fitted using equivalent circuit shown in (c). Symbols are data points. Lines are fits: BC cell (with MPL) are solid lines; BA cell (no MPL) are dashed lines. Resistance values calculated using circuit (c) are given in Table 4. (a) EIS recorded at 0.9 V ($R_2 = C_2 = 0$ in the equivalent circuit (c)). (b) EIS recorded at 1.2 A cm^{-2}. (c) Schematic of the equivalent circuit used to fit data in (a) and (b).

which was then converted to capacitance. Resistance (R) and capacitance (C) values from the equivalent circuit are listed in Table 4. The overall cell resistance can be represented as the sum of high-frequency resistance (*HFR*), kinetic resistance (K), and mass-transport resistance (*MT*), i.e. $HFR + (K + MT)$. This equivalent circuit model is a simplification that qualitatively separates the kinetic and mass-transport losses in the fuel cell and does not include a detailed analysis of the proton transport limitations in the catalyst layer (lumped into R1) or attempt to separate the mass-transport losses in the catalyst layer and the GDL (lumped into R2) [50,51]. To help interpret the impedance spectra, Fig. 8 illustrates the increase in the $(K + MT)$ resistances at 0.9 V (solid lines) and at 1.2 A cm^{-2} (dashed lines) relative to the initial resistance at BOL; $(K + MT)_{corroded}/(K + MT)_{BOL}$.

The *HFR* (Fig. 7, Table 4) remained unchanged for the BC cell, while it steadily increased in the BA cell throughout the corrosion series (~15% total). This increase in the *HFR* in the BA cell is probably due to increase in the contact resistance between the GDL fibers and the CL, caused by uneven, localized thinning of the membrane and CL (as will be illustrated at the end of Section 3.2). Note that for either cell the *HFR* did not differ when measured at 0.9 V (Table 4a) and at 1.2 A cm^{-2} (Table 4b).

Kinetic resistance is characterized by EIS at 0.9 V (Fig. 7a, Table 4a) because at this potential: $K >> MT$. EIS data were fitted with single semicircles using equivalent circuit model in Fig. 7c ($K \approx R_1$, with $R_2 = C_2 = 0$). Both cells started with similar kinetic resistances: the BOL curves overlap, which is expected given the catalyst layers are identical. Kinetic resistance remains similar for the two cells after 4–5 h. Thereafter, kinetic resistance of the BA cell increased at a higher rate. The BA resistance increases significantly from 6th to 7th corrosion hour (from ~5.7 Ω cm^2 to ~7.5 Ω cm^2), while the BC kinetic resistance remains almost identical after 6 and

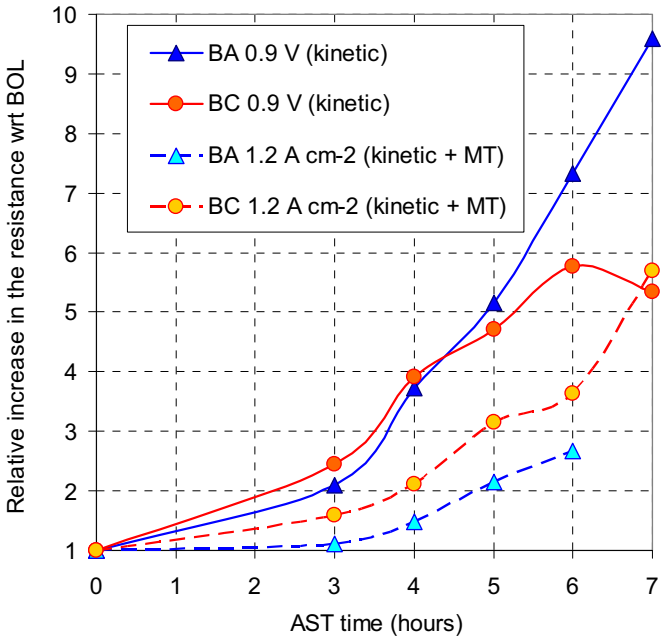

Fig. 8. Analysis of EIS data from Fig. 7. Increase in the resistance during AST relative to the BOL resistance, $(K + MT)_{corroded}/(K + MT)_{BOL}$, calculated from EIS measurements in Fig. 7 (values given in Table 4). Solid lines = 0.9 V data ($K >> MT$); dashed lines = 1.2 A cm^{-2} data.

Table 4a
Values obtained from EIS data at 0.9 V (Fig. 7a) using equivalent circuit (Fig. 7c). $K + MT = R_1$; $K >> MT$.

AST time	BC cell			BA cell		
	HFR (Ω cm^2)	R_1 (Ω cm^2)	C_1 (mF)	*HFR* (Ω cm^2)	R_1 (Ω cm^2)	C_1 (mF)
BOL	0.134	0.779	39.9	0.132	0.777	44.3
3 h	0.135	1.91	32.9	0.137	1.63	30.4
4 h	0.127	3.05	28.7	0.144	2.89	26.0
5 h	0.135	3.67	26.7	0.149	4.01	22.8
6 h	0.138	4.50	24.1	0.155	5.69	21.5
7 h	0.141	4.16	21.5	0.155	7.46	21.2

7 h of corrosion (~4.5 Ω cm^2). Accelerated kinetic resistance increase in the BA cell and the increasing divergence from the BC cell resistance beyond the 4th hour of the corrosion AST (Fig. 8, solid lines) correlates well with the trend observed in the ECSA degradation rate (Fig. 3). From the much higher kinetic resistance (and lower ECSA) of the BA cell after prolonged AST, we infer that the catalyst layer suffered higher levels of degradation than in the cell with the MPL.

Impedance spectra for the cells operating at 1.2 A cm^{-2} (mass-transport dominated regime) is given in Fig. 7b (equivalent circuit values given in Table 4b; $(K + MT) = (R_1 + R_2)$). The resistance is comprised of both mass-transport and kinetic contributions, but the absolute value of kinetic component here is lower than at 0.9 V (Fig. 7a) due to higher overpotential. Complementary plots in Fig. 8 serve to illustrate the relative change in K and MT contributions during corrosion AST. The data set at 1.2 A cm^{-2} is noisy, especially at lower frequencies. The noise is partially due to the water transport issues specific for this cell geometry.

At BOL the BC cell exhibited lower overall resistance ($K + MT$) than the BA cell (Fig. 7b), which implies a lower mass-transport resistance since the cells initially had the same kinetic resistance (Fig. 7a). However, the BC cell also showed faster increase of mass-transport resistance at the start (1–3 h) and at the end (6–7 h) of the AST corrosion series. The BC cell resistance ($K + MT$) almost doubled (from ~0.9 to ~1.7 Ω cm^2) between hours 6 and 7 (7 h not shown in Fig. 7b). The resistance ($K + MT$) was still higher in the BA cell after 6 h (~1.4 Ω cm^2, Fig. 7b and Table 4b), with the caveat that BA cell was not able to operate at 1.2 A cm^{-2} after 7 h of corrosion.

We recently employed neutron imaging to measure the liquid water profiles across the cell thickness during similar corrosion tests [42], which can help explain some of the observations in the present work. Identical MEA and GDL materials (BC and BA) were used in a small cell specially designed for high-resolution neutron imaging. A cell with the BC GDL consistently retained less water in the MEA than the BA cell, both during potential holds for corrosion AST and during cell operation at constant current density (i.e. constant water production rate). Lower degradation levels in the catalyst layer of the BC cell (corroborated from higher ECSA, Fig. 3, and lower kinetic resistance, Fig. 7a) can therefore be explained by the lower water content in the CL during potential holds. In contrast, carbon corrosion in the CL of the BA cell was faster due to more water in the CL in the absence of MPL. Per same argument, it is possible that the nonuniform degradation across the BC cell area (Fig. 5a) was caused by spatial variations in water retention in the CL during potential holds. However this could not be confirmed from neutron imaging because the cell was too small (2.5 cm^2) to exhibit a significant difference in water retention between the inlet and outlet regions. Note also that the water content in both cells substantially reduced with corrosion time [42], which was surprising since hydrophobicity loss is anticipated in corroded CL, GDL and MPL [1,14,38,39]. The main driving force for such behavior was the increased heat generation in corroded cells (as the voltage degraded at constant current operation), which overwhelmed any change in the wetting properties.

Trends in the kinetic resistance increase with BC and BA cells (Figs. 7 and 8) agree with the observations from the neutron imaging experiments [42]. However, the resistance ($K + MT$) at relatively high current (0.8 A cm^{-2}) and prolonged corrosion time in the small cell used for neutron imaging was substantially higher in the BC cell than in the BA cell, indicating that the MT contribution in the small BC cell was much higher than in the present study. The mass-transport losses with the BC cells in [42] are probably in part specific to the small cell size and design (single-serpentine flow field with wide lands). MT problems at

Table 4b
Values obtained from EIS data at 1.2 A cm^{-2} (Fig. 7b) using equivalent circuit (Fig. 7c). $K + MT = R_1 + R_2$.

AST time	BC cell					BA cell				
	HFR (Ω cm^2)	R_1 (Ω cm^2)	C_1 (mF)	R_2 (Ω cm^2)	C_2 (mF)	*HFR* (Ω cm^2)	R_1 (Ω cm^2)	C_1 (mF)	R_2 (Ω cm^2)	C_2 (mF)
BOL	0.137	0.224	402.0	0.108	62.5	0.133	0.307	301.8	0.211	45.3
3 h	0.134	0.316	301.7	0.211	41.1	0.138	0.306	267.2	0.266	35.1
4 h	0.131	0.410	227.0	0.293	40.4	0.147	0.456	151.7	0.315	22.9
5 h	0.135	0.771	97.7	0.274	30.5	0.150	0.756	106.2	0.357	25.7
6 h	0.136	0.765	131.0	0.443	30.7	0.155	0.997	92.6	0.387	40.3
7 h	0.139	1.56	69.1	0.332	36.6	–	–	–	–	–

high current associated with the MPL degradation were also reported by Owejan et al. [35]. Longer comparison experiments with carbon-supported and carbon-free catalysts, as presented in Section 3.1.1, are needed to fully understand the relationship between the carbon corrosion in the MPL and the varying *MT* loss contribution during AST. Considering that *MT* issues may occur with only a minute portion of the total corroded MPL mass, it is likely that the damage to the MPL is confined to a small MPL region. Thus, one possible scenario for the high mass-transport resistance in the BC cell is formation of a thin diffusion barrier at the MPL/CL interface caused by the collapse of pore space (and possibly loss of hydrophobicity) in both MPL and CL. The MPL may therefore introduce competing contributions to the performance degradation over prolonged corrosion periods (increased diffusion barrier vs. benefit of lower corrosion in the CL).

3.2. Ex situ characterization

Increase in the average particle size caused by the 7 h long corrosion tests is shown in Fig. 9, compared to the Pt crystallite size in new MEAs of 2.6 nm. XRD analyses were performed on samples cut from different regions of the cell to evaluate the spatial variations in Pt particle size. Cathode side of the BA cell exhibited uniform particle size of ~5.5 nm across the cell. Particle size in the BC cell's catalyst layer was lower in the upstream region, ~4.8 nm, and higher in the downstream region, ~5.2 nm. Although the variations are not large, the XRD data are consistent with the changes in current distributions during corrosion for both cells (Fig. 6). Increasingly higher local current in the inlet (i.e. upstream) region of the BC cell can be explained by the slower corrosion in that region. Nonuniform Pt size in the BC cell also indicates that the current redistribution during corrosion was caused primarily by the nonuniform degradation of the catalyst layer, rather than from the MPL (although the MPL degradation may have had an effect as well). Further, the XRD analysis shows that the Pt particle size averaged over the entire cell area increased more without the MPL (~5.5 nm) than with the MPL (~5 nm). Considering the better performance of the BC cell after corrosion (Figs. 4 and 5), the benefit of reduced degradation level in the CL in the presence of MPL (evidenced through XRD, CV, and EIS data) outweighed the mass-transport issues associated with corrosion in the MPL. Neutron imaging results [42] indicate that the slower particle growth with MPL was at least partially due to lower water content in the MEA during AST potential holds especially at the cell inlets. These results strongly suggest that use of an MPL can result in the presence of in-plane water activity gradients in the catalyst layer on the cell level, where the catalyst layer at the inlet is drier than the catalyst layer at the outlet, even during H_2/N_2 operation with saturated flows. Finally, particle growth was also observed in the anode catalyst layer, and was uniform and almost identical in both cells (particle size ~3.5 nm). Since the thickness of the anode CL remained unchanged after corrosion (Fig. 10), the increase in average particle size can be attributed mainly to the loss of smaller Pt particles to migration into the ionomer.

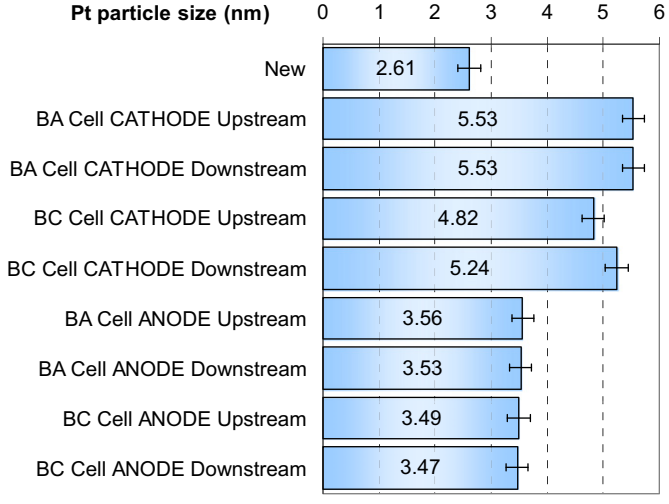

Fig. 9. Pt particle size (diameter) for BOL and after 7 h of corrosion AST (average values from multiple samples from repeated runs). Upstream region includes the top 3 rows of segments (rows 1 through 3, Figs. 1 and 6). Downstream region includes the bottom 3 rows of segments (rows 8 through 10, Figs. 1 and 6).

Cell performance is adversely affected by the changes in the CL morphology caused by carbon corrosion, mainly the collapse of pore space and Pt ECSA loss due to particle agglomeration and ripening. The loss of carbon caused by electrochemical aging weakens the porous structure of the catalyst layer. This process takes place on a carbon agglomerate level, where corrosion proceeds from the inside out, creating cavities in the agglomerates [34]. This eventually leads to the collapse of pore space, evidenced through CL thinning (Fig. 10). This process shortens the relative distances between the neighboring Pt particles thus promoting particle coalescence and sintering into larger particles. Large particles accelerate further particle growth because they serve as nuclei for Ostwald ripening, a process where smaller particles dissolve, diffuse, and redeposit onto larger particles. Both sintering and ripening are guided by minimization of surface energy, and are probably the primary mechanisms for particle growth caused by the carbon-support corrosion. Besides the increase in average Pt particle size, the result is broadening of the particle-size distribution, although not necessarily with a clear-cut shift to higher values. Corrosion will also weaken the bonds between the carbon support and anchored Pt crystallites. Some Pt particles will detach from the support and dissolve into the ionomer phase, and either reprecipitate or remain in the ionomer. Although the dissolution and reprecipitation do take place to an extent during the potential hold, they are more typical for potential cycling (AST for the catalyst). The cumulative effect of the above mechanisms is a bimodal particle size distribution in the corroded catalyst layer [1].

When analyzing the thinning of the catalyst layer, it is worthwhile to consider that the BC and BA cells lost similar amounts of carbon, with less than 75% of the original amount remaining (as measured by the NDIR data, Fig. 2, assuming an initial carbon loading of ~400 μg cm^{-2}). Images of the new and corroded MEAs are given in Fig. 10. The top row of images shows reconstructed X-ray tomographies, wherein the brighter areas correspond to higher Pt content (i.e. higher attenuation of the X-ray beam). SEM images of MEA cross-sections are displayed in the bottom row. Both GDL cases exhibited significant cathode CL thinning, while the thickness of the anode catalyst layer remained unchanged after corrosion (~7 μm). The cathode CL retained less than 1/3 of the original thickness, confirming that the catalyst-support AST caused a remarkable collapse of pore space, as suggested by the neutron imaging results [42]. The BC catalyst layer showed uniform thinning with gradual thickness variations, while the membrane thickness did not change. However, the BA cathode CL exhibited a nonuniform thinning on a length scale of 0.1 mm, affecting both the CL and the membrane. The CL thickness varied between 1 and 5 μm, with some narrow regions barely having any catalyst layer remaining. In addition, the BA cell exhibited creeping of the membrane; the membrane thinned in some areas, while it thickened in the adjacent areas. These nonuniformities in both the cathode CL and membrane of the BA

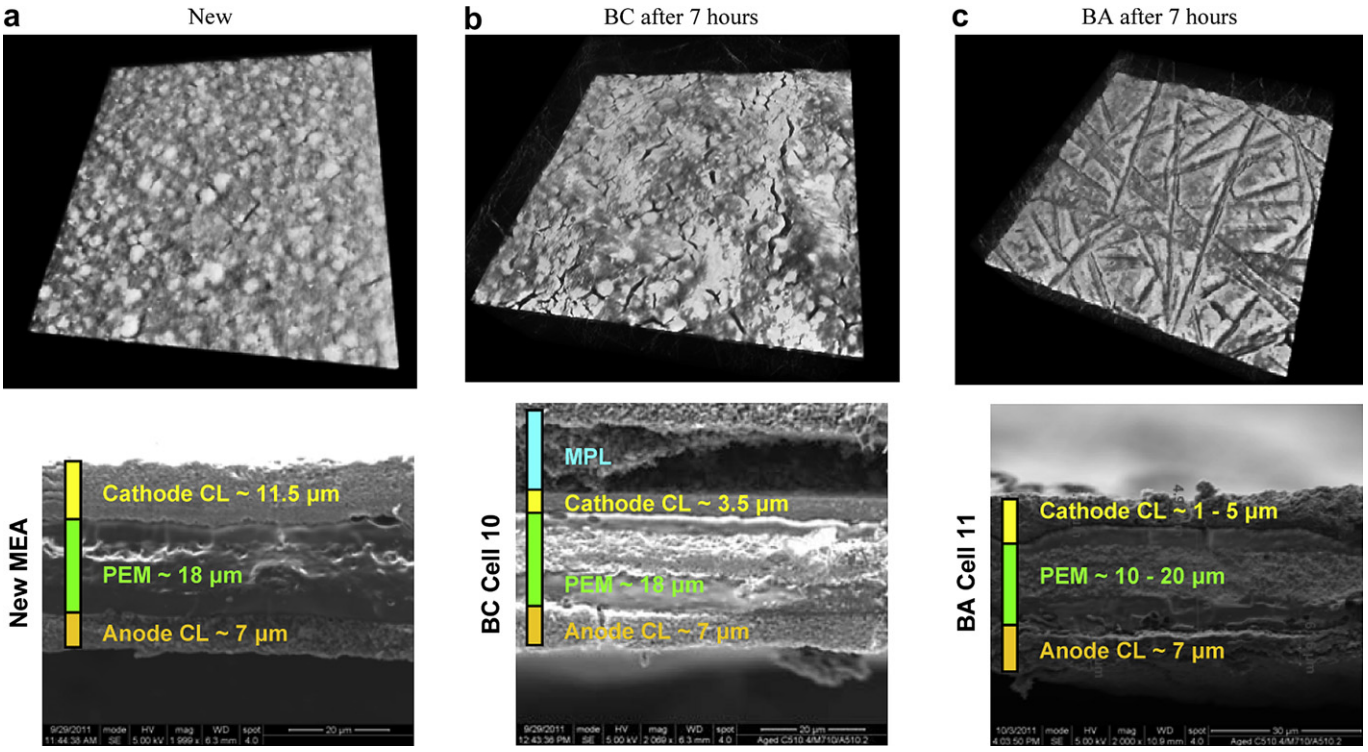

Fig. 10. Top row: Reconstructed X-ray tomographic images (area shown = 1 by 1 mm; cathode catalyst layer is on top; brighter areas correspond to higher Pt concentrations). Bottom row: SEM images of MEA cross-sections. (a) New MEA. (b) Corroded BC MEA. (c) Corroded BA MEA.

cell are likely the cause for the *HFR* increase with corrosion time (Section 3.1.3, Table 4), due to worsening contact between the GDL and the CL.

Major localized thinning of the BA cathode catalyst layer was observed in the regions where the GDL carbon fibers were in contact with the catalyst layer. While similar indentations would exist at cell operation in the absence of accelerated carbon corrosion, thinning of the cathode catalyst layer due to corrosion allows the GDL fibers to sink deeper into the catalyst layer over time. These indentations are clearly visible in the X-ray tomographic image (Fig. 10c). No such features exist in the corroded BC cell (Fig. 10b), as the MPL provides a more uniform contact with the catalyst layer. Careful inspection of the SEM cross-sectional images (Fig. 11) revealed two mechanisms responsible for the indentations. The first mechanism is dominated by mechanical compression (Fig. 11a), and is intensified by the loss of mechanical strength of the CL due to loss of carbon/pore structure. Carbon fiber is impressed onto the MEA, causing excessive thinning of both the CL and the membrane directly under the fiber. Such regions can be related to the open-circuit voltage decrease, as they are prone to crossover (Section 3.1.2). The second mechanism is dominated by carbon corrosion (Fig. 11b). Since the fibers are also regions of electrical contact with the CL, narrow region of the CL in close proximity to the fiber will experience accelerated rates of carbon loss due to corrosion, however not necessarily requiring excessive compression. Membrane thickness directly under these corroded regions of the CL remained unchanged.

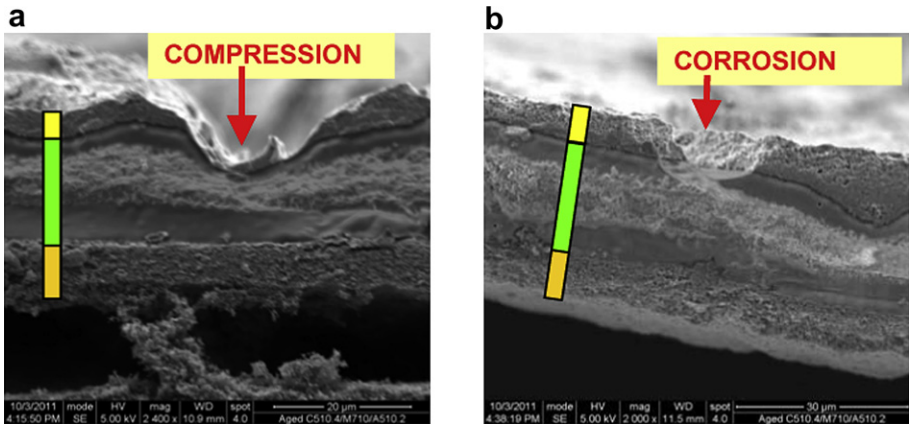

Fig. 11. SEM images showing two characteristic modes of localized cathode CL thinning in contact with the GDL carbon fibers after prolonged carbon corrosion in the BA cell. MEA components are color-coded in the same fashion as in Fig. 10. (a) Effect of compression. (b) Effect of corrosion.

4. Summary and conclusions

Performance degradation rates and mechanisms due to carbon-support corrosion were investigated in a segmented cell. The cells were aged via an AST protocol for catalyst support comprised of successive potential holds at 1.3 V in H_2/N_2 for a total period of 7 h. Spatial variations in performance degradation were measured as a function of the cathode GDL material and the AST time. The MPL effect on carbon corrosion was evaluated by characterizing the degradation using the same GDL carbon-fiber substrates with and without an MPL. The amount of carbon corroded during the AST protocol was quantified by measuring the CO_2 content in the cathode exhaust by NDIR. New and aged MEAs were subsequently subjected to *ex situ* analyses using XRD, X-ray tomography, and SEM imaging to evaluate the changes in Pt particle size, CL thickness, and material morphology.

Both GDL cases (with and without the MPL on the cathode) suffered substantial performance degradation, ECSA loss, thinning of the catalyst layer, and Pt particle growth. However, the cell with MPL was more resistant to carbon corrosion after prolonged exposure to corrosion conditions. The benefit of cathode MPL was lower degradation of the catalyst layer, evidenced by the lower kinetic losses, slower Pt particle growth, and higher remaining Pt ECSA after corrosion. Lower rates of carbon corrosion in the CL in the presence of the MPL can be explained by the lower water content in the CL during AST potential holds, measured by neutron imaging [42].

Both kinetic and mass-transport resistances were lower for the cell with the MPL after prolonged corrosion. However, the mass-transport issues may occur in the cell with the MPL, likely due to the degradation in the interfacial region of the MPL. Contribution from carbon corroded in the MPL in the collective amount of the evolved CO_2 was between 10 and 15% over short corrosion times, measured in auxiliary ASTs with carbon-supported and carbon-free CLs. Hence, while the performance degradation with the MPL was caused primarily by the corrosion in the catalyst layer, there was some contribution from corrosion in the MPL. This contribution will vary with the CL/MPL material properties, local conditions, and corrosion time.

At constant current operation, the local current for both GDL cases (and throughout the corrosion tests) decreased from inlet to outlet, which is expected for co-flow with fully humidified gases. Without the MPL, the local current densities did not change during corrosion AST, indicating uniform CL degradation across the cell area. However, the cell with MPL exhibited redistribution of current with corrosion time. The local current density increased in the inlet region, and decreased in the outlet region. This indicated that the corrosion (in the CL and/or MPL) was also nonuniform, and was higher in the outlet region. XRD analysis revealed that the nonuniform CL degradation (rather than the MPL degradation) was responsible for the change in current distribution. The region of faster (slower) Pt particle growth correlated with the region of decreased (increased) local current density. Note that the uniform Pt particle size was measured across the cell without the MPL, however it was still slightly higher than in the most degraded (i.e. outlet) region of the cell with the MPL.

Degradation responsible for performance loss includes both collapse of the CL pore structure and loss of Pt ECSA. The cell with the MPL showed spatial variation in catalyst degradation on the cell level. CL degradation on the micro level was uniform as the MPL provided better intimate contact with the CL. Conversely, the cell without the MPL experienced uniform degradation on the cell level, but suffered highly nonuniform damage at the micro-scale. Narrow regions of the CL in direct contact with the GDL carbon fibers experienced dramatic localized thinning, originated from combined effects of mechanical compression and electrochemical corrosion.

Acknowledgments

The authors gratefully acknowledge the funding from the US Department of Energy, the Office of Energy Efficiency and Renewable Energy, Fuel Cell Technologies Program, and the support of the technology development manager Nancy Garland. We thank the members of our group, especially Fernando Garzon and David Langlois for helping with XRD measurements and analysis. We also acknowledge SGL Carbon GmbH for supplying the GDL materials, and W. L. Gore and Associates, Inc. for the MEAs.

References

[1] R. Borup, J. Meyers, B. Pivovar, Y.S. Kim, R. Mukundan, N. Garland, D. Myers, M. Wilson, F. Garzon, D. Wood, P. Zelenay, K. More, K. Stroh, T. Zawodzinski, J. Boncella, J.E. McGrath, M. Inaba, K. Miyatake, M. Hori, K. Ota, Z. Ogumi, S. Miyata, A. Nishikata, Z. Siroma, Y. Uchimoto, K. Yasuda, K.-i. Kimijima, N. Iwashita, Chemical Reviews 107 (2007) 3904–3951.
[2] R.L. Borup, R. Mukundan, ECS Transactions 33 (2010) 17–26.
[3] J. Wu, X.Z. Yuan, J.J. Martin, H. Wang, J. Zhang, J. Shen, S. Wu, W. Merida, Journal of Power Sources 184 (2008) 104–119.
[4] S. Zhang, X. Yuan, H. Wang, W. Merida, H. Zhu, J. Shen, S. Wu, J. Zhang, International Journal of Hydrogen Energy 34 (2009) 388–404.
[5] N. Garland, T. Benjamin, J. Kopasz, ECS Transactions 11 (2007) 923–931.
[6] F.A. de Bruijn, V.A.T. Dam, G.J.M. Janssen, Fuel Cells 8 (2008) 3–22.
[7] R. Makharia, S. Kocha, P. Yu, M.A. Sweikart, W. Gu, F. Wagner, H.A. Gasteiger, ECS Transactions 1 (2006) 3–18.
[8] R. Mukundan, G. James, J. Davey, D. Langlois, D. Torraco, W. Yoon, A.Z. Weber, R. Borup, ECS Transactions 41 (2011) 613–619.
[9] M.L. Perry, T. Patterson, C. Reiser, ECS Transactions 3 (2006) 783–795.
[10] S. Litster, G. McLean, Journal of Power Sources 130 (2004) 61–76.
[11] E.A. Ticianelli, C.R. Derouin, A. Redondo, S. Srinivasan, Journal of the Electrochemical Society 135 (1988) 2209–2214.
[12] M.S. Wilson, S. Gottesfeld, Journal of Applied Electrochemistry 22 (1992) 1–7.
[13] P.J. Ferreira, G.J. la O, Y. Shao-Horn, D. Morgan, R. Makharia, S. Kocha, H.A. Gasteiger, Journal of the Electrochemical Society 152 (2005) A2256–A2271.
[14] K.H. Kangasniemi, D.A. Condit, T.D. Jarvi, Journal of the Electrochemical Society 151 (2004) E125–E132.
[15] M. Pourbaix, Atlas of Electrochemical Equilibria in Aqueous Solutions, Pergamon Press, Oxford; New York, 1966.
[16] L.M. Roen, C.H. Paik, T.D. Jarvi, Electrochemical and Solid-State Letters 7 (2004) A19–A22.
[17] T.W. Patterson, R.M. Darling, Electrochemical and Solid State Letters 9 (2006) A183–A185.
[18] C.A. Reiser, L. Bregoli, T.W. Patterson, J.S. Yi, J.D.L. Yang, M.L. Perry, T.D. Jarvi, Electrochemical and Solid State Letters 8 (2005) A273–A276.
[19] N. Pekula, K. Heller, P.A. Chuang, A. Turhan, M.M. Mench, J.S. Brenizer, K. Unlu, Nuclear Instruments & Methods in Physics Research Section A-Accelerators Spectrometers Detectors and Associated Equipment 542 (2005) 134–141.
[20] D. Spernjak, A.K. Prasad, S.G. Advani, Journal of Power Sources 170 (2007) 334–344.
[21] D. Spernjak, A.K. Prasad, S.G. Advani, Journal of Power Sources 195 (2010) 3553–3568.
[22] A. Lamibrac, G. Maranzana, O. Lottin, J. Dillet, J. Mainka, S. Didierjean, A. Thomas, C. Moyne, Journal of Power Sources 196 (2011) 9451–9458.
[23] J.P. Meyers, R.M. Darling, Journal of the Electrochemical Society 153 (2006) A1432–A1442.
[24] R. Sidik, Journal of Solid State Electrochemistry 13 (2009) 1123–1126.
[25] H. Tang, Z. Qi, M. Ramani, J.F. Elter, Journal of Power Sources 158 (2006) 1306–1312.
[26] P.T. Yu, W. Gu, R. Makharia, F.T. Wagner, H.A. Gasteiger, ECS Transactions 3 (2006) 797–809.
[27] R.N. Carter, W. Gu, B. Brady, P.T. Yu, K. Subramanian, H. Gasteiger, in: W. Vielstich, A. Lamm, H.A. Gasteiger (Eds.), Handbook of Fuel Cells: Fundamentals, Technology, and Applications, vol. 6, Wiley, Chichester, England, 2009.
[28] H.-S. Oh, J.-G. Oh, S. Haam, K. Arunabha, B. Roh, I. Hwang, H. Kim, Electrochemistry Communications 10 (2008) 1048–1051.
[29] G. Bender, M.S. Wilson, T.A. Zawodzinski, Journal of Power Sources 123 (2003) 163–171.
[30] S.A. Freunberger, M. Reum, F. Buchi, in: W. Vielstich, A. Lamm, H.A. Gasteiger (Eds.), Handbook of Fuel Cells: Fundamentals, Technology, and Applications, vol. 6, Wiley, Chichester, England, 2009.
[31] M. Schulze, E. Gülzow, S. Schönbauer, T. Knöri, R. Reissner, Journal of Power Sources 173 (2007) 19–27.
[32] Y. Ishigami, K. Takada, H. Yano, J. Inukai, M. Uchida, Y. Nagumo, T. Hyakutake, H. Nishide, M. Watanabe, Journal of Power Sources 196 (2011) 3003–3008.

[33] W. Gu, R.N. Carter, P.T. Yu, H.A. Gasteiger, ECS Transactions 11 (2007) 963–973.
[34] Z.Y. Liu, B.K. Brady, R.N. Carter, B. Litteer, M. Budinski, J.K. Hyun, D.A. Muller, Journal of the Electrochemical Society 155 (2008) B979–B984.
[35] J.E. Owejan, P.T. Yu, R. Makharia, ECS Transactions 11 (2007) 1049–1057.
[36] A.M. Kannan, A. Menghal, I.V. Barsukov, Electrochemistry Communications 8 (2006) 887–891.
[37] R.L. Borup, R. Mukundan, J. Davey, D.L. Wood, T.E. Springer, Y.S. Kim, J. Spendelow, T. Rockward, B. Pivovar, M. Arif, D. Jacobson, D. Hussey, K.S. Chen, K. More, P.M. Wilde, T. Zawodzinski, V. Gurau, W. Johnson, S. Cleghorn, 2007 DOE Hydrogen Program Review, Arlington, VA, (2007).
[38] G. Chen, H. Zhang, H. Ma, H. Zhong, International Journal of Hydrogen Energy 34 (2009) 8185–8192.
[39] T. Ha, J. Cho, J. Park, K. Min, H.-S. Kim, E. Lee, J.-Y. Jyoung, International Journal of Hydrogen Energy 36 (2011) 12427–12435.
[40] L.R. Jordan, A.K. Shukla, T. Behrsing, N.R. Avery, B.C. Muddle, M. Forsyth, Journal of Power Sources 86 (2000) 250–254.
[41] J.D. Fairweather, B. Li, R. Mukundan, J. Fenton, R.L. Borup, ECS Transactions 33 (2010) 433–446.
[42] J.D. Fairweather, D. Spernjak, R. Mukundan, J. Spendelow, K. Artyushkova, P. Atanassov, D.S. Hussey, D.L. Jacobson, R. Borup, ECS Transactions 41 (2011) 337–348.
[43] S. Maass, F. Finsterwalder, G. Frank, R. Hartmann, C. Merten, Journal of Power Sources 176 (2008) 444–451.
[44] R. Mukundan, J. Davey, J.D. Fairweather, D. Spernjak, J.S. Spendelow, D.S. Hussey, D. Jacobson, P. Wilde, R. Schweiss, R.L. Borup, ECS Transactions 33 (2010) 1109–1114.
[45] F.H. Garzon, J. Davey, R. Borup, ECS Transactions 1 (2006) 153–166.
[46] F.H. Garzon, S.H. Lau, J.R. Davey, R. Borup, ECS Transactions 11 (2007) 1139–1149.
[47] K.G. Gallagher, D.T. Wong, T.F. Fuller, Journal of the Electrochemical Society 155 (2008) B488–B493.
[48] D. Natarajan, T. Van Nguyen, Journal of Power Sources 115 (2003) 66–80.
[49] C.H. Hsu, F. Mansfeld, Corrosion 57 (2001) 747–748.
[50] R. Makharia, M.F. Mathias, D.R. Baker, Journal of the Electrochemical Society 152 (2005) A970–A977.
[51] X. Yuan, H. Wang, J. Colin Sun, J. Zhang, International Journal of Hydrogen Energy 32 (2007) 4365–4380.